

High Resolution Calculations of Merging Neutron Stars I: Model Description and Hydrodynamic Evolution

S. Rosswog, M.B. Davies

Department of Physics and Astronomy, University of Leicester, LE1 7RH, Leicester, UK

arXiv:astro-ph/0110180v1 8 Oct 2001

Accepted YEAR MONTH DAY. Received YEAR MONTH DAY; in original form YEAR MONTH DAY

ABSTRACT

We present the results of 3D high resolution calculations of the last inspiral stages and the final coalescence of neutron star binary systems. The equations of hydrodynamics are solved using the smoothed particle hydrodynamics method with up to 10^6 particles. Using Newtonian gravity, but adding the forces emerging from the emission of gravitational waves, we focus on the impact of microphysics on the dynamical evolution of the merger. Namely we use a new equation of state based on the one provided by the relativistic mean field approach of Shen et al. (1998a,b). Neutrino emission of all flavours, and the resulting cooling and, the change in the electron fraction is accounted for with a detailed leakage scheme.

The new equation of state is substantially stiffer than the Lattimer-Swesty equation of state that has been used in previous investigations. This leads the system to become dynamically unstable at a separation as large as 3.3 stellar radii, where the secular orbital decay undergoes a transition towards a dynamical “plunge” of the binary components towards each other. As soon as the stars come into contact a Kelvin-Helmholtz-instability forms at the interface of both stars. The peak temperatures are found in the vortex rolls that form during this process. We generally find slightly lower temperatures than previously found using the Lattimer-Swesty equation of state. The temperatures in the disk that forms around the central object, for example, reach peak values of only 2-3 MeV, a fact that we attribute mainly to the larger stiffness of the equation of state in this density regime. These conditions allow for the existence of heavy nuclei even in the inner parts of the disk, we find typical mass fractions of ~ 0.1 , which is enough for scattering off heavy nuclei to be the dominant source of neutrino opacity.

The central object formed during the coalescence shows a rapid, differential rotation with periods of ~ 2 ms. Although a final conclusion on this point is not possible from our basically Newtonian approach, we argue that the central object will remain stable without collapsing to a black hole, at least on the simulation time scale of 20 ms, mainly stabilized by differential rotation. This can wind up initial magnetic fields to $\sim 10^{17}$ G (Duncan & Thompson 1992) and therefore may have important implications for this event as a central engine of Gamma Ray Bursts.

Key words: dense matter; hydrodynamics; neutrinos; gamma rays: bursts; stars: neutron; methods: numerical

1 INTRODUCTION

The final stage of the inspiral and the subsequent coalescence of a neutron star binary system is among the prime candidates for ground based gravitational wave detection via the laser interferometers currently under construction such as LIGO (Abramovici et al., 1992), TAMA (Kuroda et al., 1997), VIRGO (Bradaschia et al., 1990) and GEO (Danzmann, 1997). The neutron star merger scenario could also

provide the energy reservoirs to power cosmological gamma ray bursts (GRB; Paczyński (1986); Eichler et al. (1989)) and is in addition one of the two most discussed production sites of the heavy, rapid neutron capture elements (Lattimer & Schramm, 1974, 1976; Symbalisty & Schramm, 1982; Eichler et al., 1989; Rosswog et al., 1999; Freiburghaus et al., 1999). Whether this scenario can fulfil all these promises or not, neutron star binary systems are known to exist and to inevitably coalesce (Taylor, 1994). This fact alone - apart

from all further promises - justifies a careful study of the coalescence process and its possible implications.

The coalescence is an intrinsically three-dimensional phenomenon and therefore analytical guidance is rare although very welcome and one has to resort to large scale computations. Additional complications arise from the fact that there is almost no field of astrophysics that does not enter at some stage during the coalescence process: the last stages and the merger are certainly dominated by strong-field general relativistic gravity, the neutron star material follows the laws of hydrodynamics, particle physics enters via possible condensates of "exotic" matter in the high-density interiors of the neutron stars and the copiously produced neutrinos in the hot and dense neutron star debris, questions concerning element formation require detailed information on nuclear structure and reactions (often far from stability) to be included and also magnetic fields might play a decisive role since they may, via transport of angular momentum, determine whether and/or when the central, coalesced object collapses into a black hole.

Due to this complexity current investigations follow one of two "orthogonal" lines: either ignoring microphysics, resorting to the simplest, although unphysical equations of state (EOS), polytropes, and thereby focussing on solving the complicated set of general relativistic fluid dynamics (or some approximation to it) or using Newtonian self-gravity of the fluid and investigating the influences of detailed micro-physics and relating the event to astrophysical phenomena. Many groups have performed 3D calculations of the merger scenario. The first work, using a polytropic EOS and Newtonian gravity, was performed by Oohara & Nakamura (1997, and references therein) using Eulerian finite difference codes. Rasio & Shapiro (1992, 1994, 1995), Zhuge et al. (1994, 1996) and Davies et al. (1994) have used the smoothed particle hydrodynamics method (SPH) to further explore various aspects of the scenario.

The strong-field gravity aspect of the event was explored again by Oohara & Nakamura (1997, and references therein) using Post-Newtonian hydrodynamics in Eulerian formulation. Recently, Post-Newtonian calculations have also been performed using SPH by Ayal et al. (2001), Faber & Rasio (2000) and Faber et al. (2001). Several groups have worked on general relativistic formulations where the metric has been treated in the conformal flatness approximation (Wilson & Mathews, 1995; Oohara & Nakamura, 1997; Baumgarte et al., 1997; Oechslin et al., 2001). Recently, much progress has been made towards a stable implementation of the fully relativistic equations of hydrodynamics (Shibata, 1999; Shibata & Uryu, 2000).

The line relying on (basically) Newtonian gravity and investigating the microphysics of the event has been explored by Ruffert et al. (1996, 1997) and Ruffert & Janka (2001) using a grid based PPM-code and by Rosswog et al. (1999, 2000) using SPH.

In this paper we want to further explore the last line, i.e. the impact of the microphysics on the outcome of the coalescence. We use a new equation of state that overcomes previous restrictions in the temperature and density. Since the high density regime of the nuclear physics is only poorly known to date this work will unfortunately not provide the final answer, but further broaden our understanding of the large effects that can be expected from the nuclear physics

input. The calculations to be described below were performed on parallel computers allowing for an unprecedented hydrodynamic resolution.

The paper is organized as follows. In Section 2 we describe the basic ingredients like the hydrodynamics or the equation of state of our model. Section 3 describes the initial conditions of our calculations, the overall hydrodynamic evolution, and then focusses on aspects concerning the central object and the debris, referred to as "disk". A summary and discussion are provided in Section 4.

2 MODEL

2.1 Hydrodynamics

To follow the dynamical evolution of the neutron star fluid we use a Lagrangian particle scheme, the so-called smoothed particle hydrodynamics method (SPH; Benz (1990); Monaghan (1992)). Since it is independent of any prescribed geometry (e.g. grid) it is perfectly suited to handle the intrinsically three-dimensional merger process. In addition, the Lagrangian nature of the scheme makes it easy to carefully track the evolution of interesting portions of the fluid (e.g. possible ejecta). Voids are treated in a natural way (i.e. no particles) and do not present any difficulty for the method, the interesting parts of the simulation do not have to be embedded in an artificial background medium like in other methods (e.g. PPM). The use of a background medium leads to further difficulties like emerging (artificial) shock waves at the stellar surfaces that have to be treated by additional remedies (Ruffert & Janka, 2001). If the corresponding parameters are not chosen carefully, the artificial medium may also lead to a damping of (physical) oscillations (Font et al., 2000).

Since SPH is well-known we will only describe the basic ingredients of our code. The basic set of equations may be found in Benz (1990). Rather than the "standard" form of *artificial viscosity* (AV; Monaghan & Gingold (1983)) we use a hybrid method that profits from two improvements: the viscosity parameters are time dependent (Morris & Monaghan, 1997) and have non-negligible values only in the presence of shocks. Additionally, a switch is applied that suppresses spurious forces in pure shear flows (Balsara, 1995). This hybrid method (Rosswog et al., 2000) has been shown to resolve shocks with the same accuracy as the standard formulation of AV, but exhibits much better behaviour in shear flows. In test calculations of differentially rotating stars the viscous time scales $\tau_{visc,i} = v_i/v_{i,visc}$ obtained with the new scheme were two orders of magnitude longer than those from the standard form of AV. For details and test calculations we refer to Rosswog et al. (2000). The (Newtonian) forces of the *self-gravity* of the fluid are efficiently calculated using a binary tree (Benz et al., 1990). Since the computationally most expensive part of the code is the evaluation of gravitational forces we implemented an *integrator* for the set of differential equations that only needs one force evaluation per time step. We decided to implement an Adams-Bashforth method which is third order accurate in time. This allows for a very accurate conservation of energy and angular momentum even with relative large step sizes. In a calculation with $\sim 100\,000$ particles these quantities are conserved to

a few times 10^{-4} over ~ 10000 time steps. For reasons of comparison: other schemes (Ruffert & Janka, 2001) lose up to 10 % of the total angular momentum by numerical artifacts despite excellent energy conservation.

Our whole code is parallelized for use on shared memory machines using OpenMP. For particle numbers above $\sim 400\,000$ we find an almost linear speedup for up to 120 processors.

2.2 Gravitational Wave Backreaction

The forces emerging from the emission of gravitational waves that drive the binary towards coalescence are treated in the point mass limit of the quadrupole approximation and are described in detail in Rosswog et al. (1999). Since the same backreaction acceleration is applied to each particle within one star the conservation of the fluid circulation is guaranteed. For a further discussion of this approach we refer to Rosswog et al. (1999).

2.3 Equation of State

The equation of state (EOS) is one of the most crucial ingredients of a neutron star simulation and the microscopic behaviour of matter decisively determines the overall, macroscopic evolution of the system (compare, for example, the calculations using a polytrope versus those with the nuclear EOS of Lattimer & Swesty (1991) [LS-EOS] in Rosswog et al. (1999)). Since the stiffness of the EOS varies over a wide range as a function of density, temperature and composition (see below) and the release of nuclear binding energy when nucleons form nuclei has important dynamical consequences, a simple polytropic EOS is only a poor approximation of the involved microphysics. All neutron star merger calculations that used a nuclear equation of state (Ruffert et al., 1996, 1997; Rosswog et al., 1999, 2000) relied on the Lattimer-Swesty-EOS. This EOS, however, has been designed for the use in supernova-calculations and therefore suffers from some deficiencies in our context: the electron fraction, Y_e , is restricted to values above ~ 0.04 , temperatures to values above $\sim 10^9$ K and densities above 10^7 g cm $^{-3}$. The electron fraction in a neutron star in beta-equilibrium, however, dips down to values of ~ 0.01 near the neutron star surface (see below) and temperatures in old neutron stars are expected to be negligible with respect to typical nuclear energies; viscous heating during the inspiral is expected to increase the temperatures to only $\sim 10^8$ K (Lai, 1994). Therefore, once outside the EOS-range, these investigations either used extrapolation (Ruffert et al., 1996) or kept the EOS-quantities at the boundary values (Rosswog et al., 1999).

In this work we use an EOS that is based on the tables of Shen et al. (1998a,b) that overcomes all above mentioned restrictions, in the electron fraction as well as in temperature and density. Shen et al. follow a relativistic mean field (RMF) approach which reproduces the basic features of more complicated relativistic Dirac-Brückner-Hartree-Fock calculations. The starting point is a relativistically covariant lagrangian that contains, apart from the nucleon fields, the scalar σ , the vector ω and the tensor ρ mesons. For the σ and ω meson fields non-linear terms are included, which

are essential to reproduce quantitative properties of nuclei (e.g. the compression modulus) correctly. The parameter set (TM1, Sugahara & Toki (1994)) is chosen in a way that experimental data of finite nuclei in the ground as well as in excited states are satisfactorily reproduced. With this parameter set the compression modulus, K_0 , has a value of 281 MeV, whereas in the Lattimer and Swesty EOS in Ruffert et al. (1996) and Rosswog et al. (1999) $K_0 = 180$ MeV has been used. Since many-body interactions at high densities are only poorly constrained to date no effort is made to include more “exotic” physics such as hyperons, various mesons or quark matter in the high density regime.

At densities above $\sim 1/3 \rho_{nuc}$ protons and neutrons form a homogeneous “nucleon fluid”, below this density matter may become inhomogeneous, i.e. the presence of nuclei may become energetically favorable. This phase is modelled using the Thomas-Fermi approximation. Matter is assumed to consist of a mixture of nucleons, alpha-particles and spherical nuclei arranged on a lattice. The heavy nucleus (representative of a distribution of heavy nuclei) is assumed to be centered in a charge neutral cell consisting of vapor of the neutrons, protons and alpha particles. Above $\rho \approx 10^{10}$ g cm $^{-3}$ the nucleons are treated by the RMF theory, below this density they are assumed to form a Maxwell-Boltzmann gas. The alpha-particles are treated as a non-interacting Boltzmann gas, their occupied volume is accounted for in the calculation of the free energies. The density distribution in the Wigner-Seitz cell is parametrized and the free parameters are determined by minimizing the free energy density with respect to the densities of all ingredients.

Shen et al. only provide the baryonic part of the EOS. Their tables range from 0 to 100 MeV in temperature, 0 to ~ 0.56 in Y_e and 5.1 to 15.4 in $\log(\rho)$ (ρ in cgs-units). We therefore add the contributions from photons and electron-positron pairs to the baryonic components. For the electron-positron pairs we use the code of Timmes & Arnett (1999). Apart from disregarding interactions, which is perfectly justified at the high densities of interest, the electron-positron-pairs are treated in full generality without any approximation. In the low density regime, $\rho < 10^5$ g cm $^{-3}$, we extend the EOS with a gas consisting of neutrons, alpha-particles, electron-positron pairs and photons. The smooth transition is demonstrated in Figure 1. The EOS described above is tabulated with 32 entries in temperature, 72 in electron fraction and 151 in density. We store the following quantities: total pressure, internal energy, difference in the nucleonic chemical potentials $\hat{\mu}$, sound velocity, entropy, mass fractions of protons (x_h), alpha particles (x_α) and the heavy nucleus (x_h), the proton to nucleon ratio, Z/A , and the nucleon number A of the heavy nucleus. The neutron mass fraction is obtained as $x_n = 1 - (x_p + x_\alpha + x_h)$.

In Fig. 2 we show a comparison between the pressures provided by both the LS-EOS and the EOS of Shen et al. Below 10^{11} g cm $^{-3}$ the results are practically identical, at higher densities the new EOS is substantially stiffer than the LS-EOS. For rather low temperatures ($T = 1$ MeV) we find large differences in the density range from 10^{12} to 10^{14} g cm $^{-3}$, which is the density regime that is crucial for the torus that forms around the central object, see below. For even higher densities the pressure curves for different temperatures converge indicating the diminishing relevance of thermal pressure contributions. Again, the Shen et al. EOS

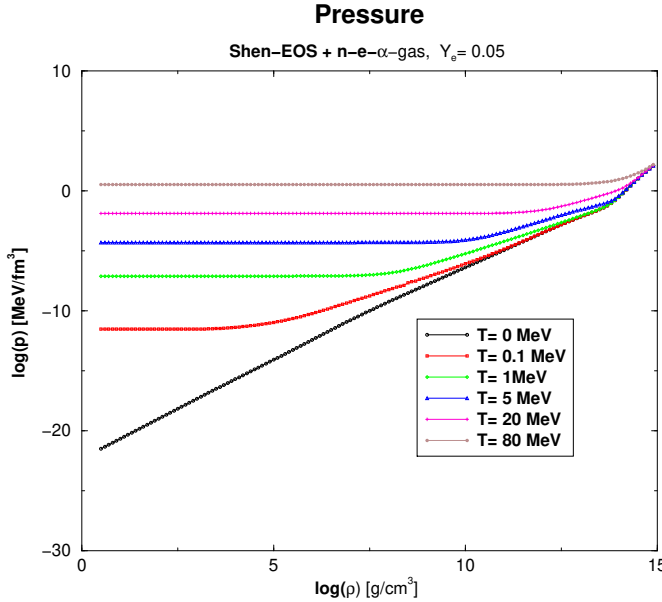


Figure 1. Pressure as a function of temperature for our EOS (baryonic part from Shen et al. + photons + electron-positron pairs, extension with a gas consisting of neutrons, alpha particles, electron-positron pairs and photons).

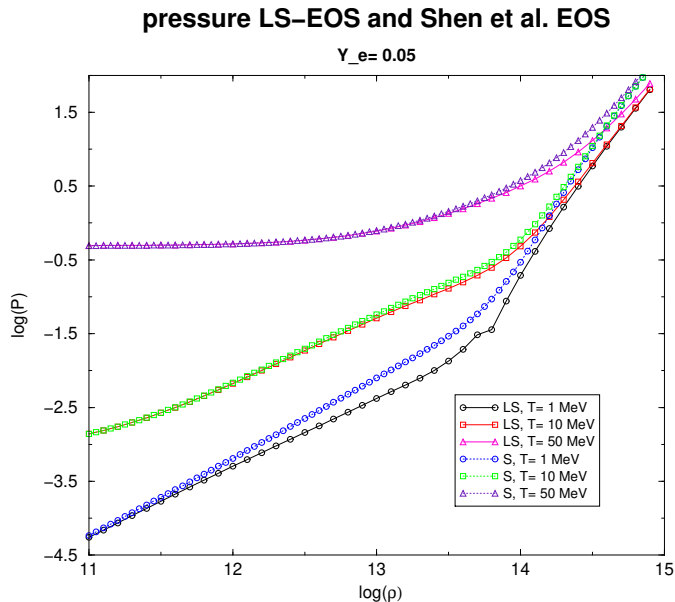


Figure 2. Comparison of the pressures provided by the Lattimer-Swesty and the Shen et al. EOS.

yields considerably higher pressure values.

The Shen-EOS also yields larger values for $\hat{\mu}$. Since the neutrinoless β -equilibrium value of the electron chemical potential is given by $\bar{\mu}_e = \hat{\mu} - Q$, Q being the neutron proton mass difference, and Y_e is a monotonic function of $\bar{\mu}_e$ the Shen-EOS yields higher values for Y_e than the LS-EOS.

2.4 Neutrino Physics

The emission of neutrinos provides a very efficient cooling mechanism for hot neutron star matter and the related elec-

tron and positron captures change the electron fraction Y_e which in turn determines the matter composition. We include the most important neutrino reactions where we ensure, via effective rates, that only the amount of neutrinos is produced that is actually able to leave the dense surrounding material. Our scheme takes careful account of the energy dependence of the neutrino opacities by integrating over the neutrino distributions.

For the emission processes we include electron captures (EC)

$$e^- + p \rightarrow n + \nu_e \quad (1)$$

and positron captures (PC)

$$e^+ + n \rightarrow p + \bar{\nu}_e \quad (2)$$

which produce electron flavour neutrinos and the pair producing reactions, pair annihilation

$$e^- + e^+ \rightarrow \nu_i + \bar{\nu}_i \quad (3)$$

and plasmon decay

$$\gamma \rightarrow \nu_i + \bar{\nu}_i. \quad (4)$$

Here $\bar{\nu}_i/\nu_i$ refer to anti-/neutrinos of all types.

For the opacities we include the dominant processes, neutrino nucleon scattering

$$\nu_i + \{n, p\} \rightarrow \nu_i + \{n, p\}, \quad (5)$$

coherent neutrino nucleus scattering

$$\nu_i + A \rightarrow \nu_i + A, \quad (6)$$

and neutrino absorption by nucleons

$$\nu_e + n \rightarrow p + e^- \quad (7)$$

$$\bar{\nu}_e + p \rightarrow n + e^+. \quad (8)$$

Note that this is the first time that the effects of scattering off heavy nuclei have been accounted for in a neutron star merger calculation. These are important whenever nuclei are present since the corresponding cross sections scale proportional to A^2 and $A \approx 80$ (see below). For details of this transport scheme we refer to the appendix of Rosswog et al. (2001), where the neutrino emission results are discussed in detail.

3 RESULTS

3.1 Initial Conditions

3.1.1 Neutron Star Masses

We focus in this investigation on equal mass systems with $1.4 M_\odot$ per star since all well-determined neutron star masses from radio binary pulsars are distributed according to a narrow distribution around $1.4 M_\odot$ (Thorsett & Chakrabarti, 1999). For neutron stars in X-ray binary systems substantially higher masses have been claimed: e.g. $1.8 \pm 0.2 M_\odot$ for CygX-2 (Orosz & Kuulkers, 1999), $\sim 1.9 M_\odot$ for VelaX-1 (J.H. van Kerkwijk & Zuiderwijk, 1995) and $1.8 \pm 0.4 M_\odot$ for 4U 1700-37 (Heap & Corcoran, 1992). In order to get an upper limit we additionally explore the case of twice $2.0 M_\odot$ (see Table 1).

It should be noted that the system dynamics is extremely sensitive to even small deviations from a mass ratio of unity.

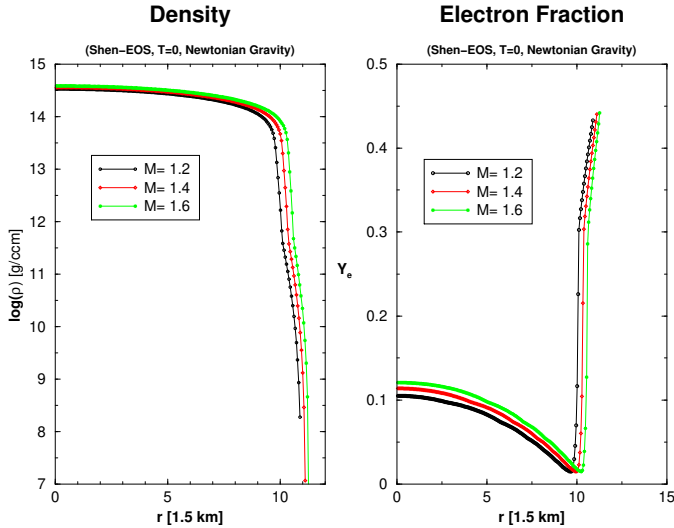


Figure 3. Profiles of matter density and electron fraction of the initial neutron star models (masses in solar units).

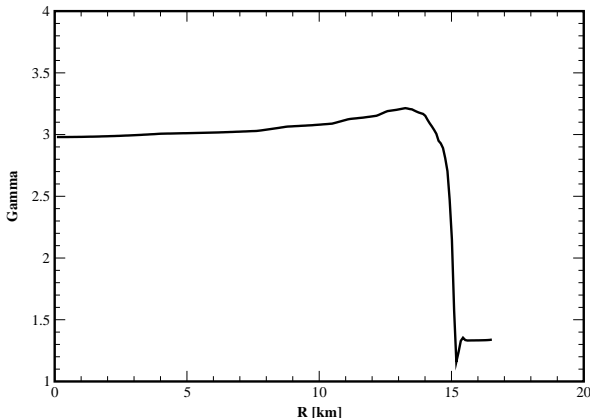


Figure 4. $\tilde{\Gamma} = \text{dln}(p)/\text{dln}(\rho)$ along a neutron star profile of $1.4 M_{\odot}$.

This sensitivity to the mass difference has been explored previously, both using a polytropic (Rasio & Shapiro, 1994) and a realistic EOS (Rosswog et al., 2000; Ruffert & Janka, 2001) and will not be the subject of this investigation.

3.1.2 Neutron Star Models

We solve the one dimensional hydrostatic structure equations together with the neutrinoless β -equilibrium condition to find the properties of the initial neutron stars. Examples of such initial profiles are shown in Fig. 3. Note the enormous density decrease at the neutron star surface which is caused by the stiffness of the Shen-EOS. To illustrate this stiffness we show in Fig. 4 the quantity $\tilde{\Gamma} = \text{dln}(p)/\text{dln}(\rho)$ obtained by finite differencing along a neutron star profile of $1.4 M_{\odot}$. $\tilde{\Gamma}$ rises from values close to 3 in the center to ~ 3.2 to drop sharply at the phase transition towards inho-

mogenous matter and remain around 1.3 in the neutron star crust.

The electron fraction, Y_e , decreases from central values around 0.1 (higher values are encountered for more massive stars) to values as low as ~ 0.01 to increase steeply again towards the surface. Note that only a tiny amount of material, $\sim 1\%$ of the star's mass, is located in this region of increasing Y_e .

3.1.3 Initial Spins and Separation

Since the time during which the neutron stars can tidally interact is extremely short it would need an implausibly high neutron star viscosity to lead to a tidal locking of the binary components during the inspiral phase (Bildsten & Cutler, 1992; Kochanek, 1992). The spins at the moment of merger will be negligible with respect to the orbital angular momentum and therefore the most realistic spin configuration is close to the irrotational case. Thus, the most configuration to be explored is the case without initial neutron star spins. We also investigate corotating systems for reasons of completeness and since it is straightforward to construct equilibrium configurations by damping out velocities in the corotating frame. For details of this procedure we refer to Rosswog et al. (1999). The case of neutron stars spinning in the direction opposite to the orbit has been explored in previous work (Ruffert et al., 1996; Rosswog et al., 1999) and shall not be further discussed here.

The neutron stars with the corresponding spins are then set to Keplerian orbits and are provided with radial velocities corresponding to

$$\dot{a}_0 = -\frac{64}{5} \frac{G^3}{c^5} \frac{M^2 \mu}{a_0^3}, \quad (9)$$

where a_0 is the initial separation, M the total and μ the reduced mass (e.g. Shapiro & Teukolsky (1983)). For further details we refer to Rosswog et al. (1999). Starting with spherical stars is obviously not an equilibrium configuration and will therefore result in oscillations of the stars. We have tried to reduce these oscillations by stretching the stars according to the ellipsoidal approximation of Lai et al. (1994a) for polytropes of $\Gamma = 3$ (compare Fig. 4) and correcting for the finite size effects in the corresponding orbital frequency. However, this did not improve the calculations, which underlines that polytropes are only poor approximations to a realistic EOS. We therefore started the calculation with spherical stars and Keplerian orbital frequency. At the chosen initial separation (see below) the tidal deformations of the stars are very small, the height of the tidal bulge being $h \approx (R_*/a_0)^3 R_* \approx 0.03 R_*$, where R_* is the neutron star radius.

The initial separation has to be determined as a tradeoff between computational resources and physically reasonable initial conditions. Binary systems can become dynamically unstable (i.e. they coalesce on a *dynamical* time scale) due to entirely Newtonian tidal effects (Chandrasekhar, 1975; Tassoul, 1975). This means that orbital decay changes abruptly from the secular orbital decay driven by the emission of gravitational waves to a rapid plunging of both components towards each other on just the orbital time scale. The reason for this instability is the steeping of the effective interaction potential between both components due to tidal effects.

Table 1. Summary of the different runs (a_0 : initial separation; ν : neutrino physics; T_{sim} : simulated duration)

run	spin	M ₁	M ₂	# part.	a_0 [km]	ν	T_{sim} [ms]
A	corot.	1.4	1.4	207,918	48	no	10.7
B	corot.	1.4	1.4	1,005,582	48	no	10.8
C	irrot.	1.4	1.4	383,470	48	yes	18.3
D	corot.	1.4	1.4	207,918	48	yes	20.2
F	irrot.	2.0	2.0	750,000	48	yes	8.1

Tidal effects increase with the incompressibility of the stellar fluid (since the stars are less centrally condensed) and therefore the onset of this dynamical instability is a very sensitive function of the stiffness of the EOS, setting in at larger separations for a stiffer EOS. This instability has been studied extensively in Newtonian gravity using an ellipsoidal approximation to the neutron star shape (Lai et al. (1994a) and references therein). Relativistic effects shift the innermost stable circular orbit, R_{ISCO} , to larger binary separations (Baumgarte et al., 1998a,b).

We determined the binary separation where the system becomes dynamically unstable experimentally. To this end a binary configuration was relaxed in the mutual tidal field, set to a corotating orbit and evolved for several orbits without radial velocity and backreaction force. This experiment again underlined the enormous stiffness of the EOS which translated in a (for a Newtonian calculation) very large separation for the ISCO. We found a corotating binary to be stable for an initial separation of $R_{dyn} = 49.5$ km, corresponding to $R_{ISCO}/R_* \approx 3.3$. We therefore chose the initial separation for the simulation start as $a_0 = 48$ km, which we regard to be an acceptable compromise between computational effort and physical appropriateness.

The simulations performed are summarized in Table 1. We use particle numbers up to 10^6 which translates into smoothing lengths of ≈ 0.38 km in the initial neutron stars.

3.2 Overall Hydrodynamic Evolution

Since we start our simulation just inside the last stable orbit the neutron stars approach each other very quickly and merge within a few orbital revolutions. Being constantly kept back by a slowly receding centrifugal barrier the merger itself proceeds very subsonically.

The corotating systems (runs A, B, D) merge within approximately one orbital period. Prior to merger only a tiny lag angle develops between the axes of the neutron stars (first panel, left column Fig. 5). Note that such a lag angle develops even in absence of viscosity since the system is not able to adapt fast enough to the rapidly changing tidal potential (Lai et al., 1994b). Immediately after contact mass shedding via the outer Langrangian points sets in which results in thick, puffed up spiral arms (Fig. 5), that subsequently wrap around the central object to form a disk. The spiral arms show an appreciable lateral expansion and soon engulf the central object and the innermost high-density parts of the disk (last panel, left column in Fig.5).

The irrotational configurations merge slightly more quickly, the system with twice $1.4 M_\odot$ (run C) after around three-quarters of an orbit and the system with $2.0 M_\odot$ (run F)

after half an orbit, due to the lower total angular momentum. This faster inspiral leads to noticeably larger lag angles before contact. The systems start immediately to shed hot material with rather low density from the interaction region. This is closely followed by mass shedding via the outer Langrangian points. The matter shedded by the latter mechanism whips through the previously ejected material forming a spiral shock which heats up the material. The spiral pattern is much less pronounced than in the corotating case and becomes washed out within a few milliseconds by lateral expansion and a rapidly expanding disk is left behind. The material within this disk follows eccentric trajectories and once the outward motion is reversed and matter starts falling back towards the hot compact remnant in the centre the inner parts of the torus become compressed and heat up. Note that in both cases the typical diameter of the mass distribution increases from ~ 100 km to ~ 1000 km in just a few milliseconds.

One may speculate that the stronger general relativistic gravity would lead to a more compact post-merger configuration with a more massive central object and a less massive torus around it. For polytropic calculations this tendency is indeed visible Shibata & Uryu (2001).

3.3 Central Object

The central objects of all performed calculations do not become axisymmetric on the simulation time scale (Figs. 5,6,7) and will therefore continue to emit gravitational radiation. This result is in qualitative agreement with those from uniformly rotating stiff polytropes ($\Gamma > \Gamma_{crit} \approx 2.3$; Tassoul (2001)). Note that contrary to previous investigations (Davies et al., 1994; Rasio & Shapiro, 1994) we never end up with rigidly rotating central objects. This is an effect from the lower viscosity due to the different artificial viscosity scheme and the high resolution of the present calculations.

It has been pointed out previously by various authors (Ruffert et al., 1996; Rosswog et al., 1999; Rasio & Shapiro, 1999; Faber et al., 2001) that a vortex sheet forms between the stars as soon as they come into contact. This is most pronounced for the irrotational case, since, in the frame corotating with the binary, the stars seem to be spinning in opposite directions and therefore a discontinuous velocity field is encountered when the interface between both stars is crossed. Such a vortex sheet is known to be Kelvin-Helmholtz unstable on all wave lengths, with the shortest modes growing fastest. As has been pointed out previously, the shortest growing mode is determined by the smallest, numerically resolvable length scale. For a further discussion of this point

Figure 5. Mass distribution in the orbital plane. The labels indicate contours of $\log(\rho)$, ρ is in g cm^{-3} . The left column corresponds to a corotating system (more than 10^6 particles, run B) the right one to a system without initial neutron star spins (more than 700 000 particles, run F).

Table 2. Final rest mass distribution, M_{co} refers to the mass of the central object and M_{deb} the mass of the debris material. a_{stab} denotes the stability parameter J/M_{co}^2 , where J is the angular momentum contained in the central object.

run	M_{co}	M_{deb}	a_{stab}
A	2.33	0.47	0.48
B	2.35	0.45	0.49
C	2.55	0.25	0.64
D	2.33	0.47	0.48
F	3.71	0.55	0.55

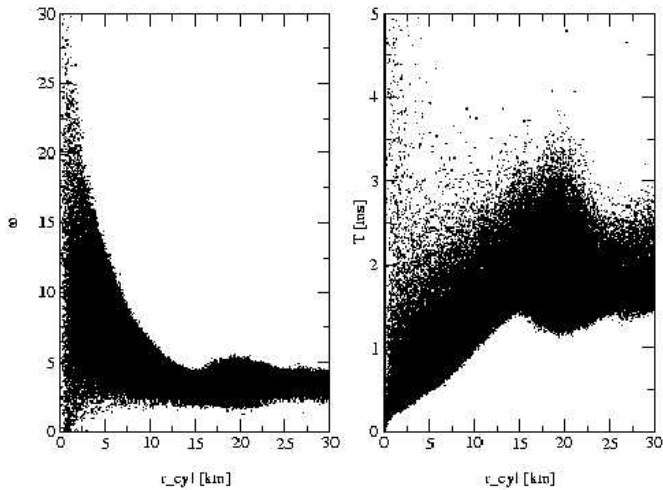


Figure 8. Left panel: snapshot of the angular frequencies, ω_i as a function of the cylindrical radius of the most realistic initial configuration, run C, at $t = 7.686$ ms, compare Fig. 7. The corresponding periods are shown in the right panel.

we refer to the previously mentioned literature.

The velocity field for the initially corotating system is shown in column one in Fig. 6. Along the vortex sheet two vortices form which remain well-separated and which are not dissipated until the end of the simulation. In Fig. 7 the velocity fields in a frame corotating with the binary system are shown (orbital plane, central object only) for the spinless system. The forming velocity discontinuities are clearly visible in the first panels of Figs. 6 and 7. The Kelvin-Helmholtz instability creates a set of vortices along the interaction interface. The latter merge during the further evolution leaving behind a differentially rotating central object with the *core of the merged remnant spinning in opposite direction to the crust* (in the corotating frame). As will be discussed below, this may have important consequences for the stability of the central object.

In Fig. 8, left panel, we show a snapshot of the angular frequencies, ω_i , of the particles within the central object of run C at $t = 7.686$ ms (last panel, column one, Fig. 7). The right panel shows the corresponding periods.

It is inside the vortices that the highest temperatures of

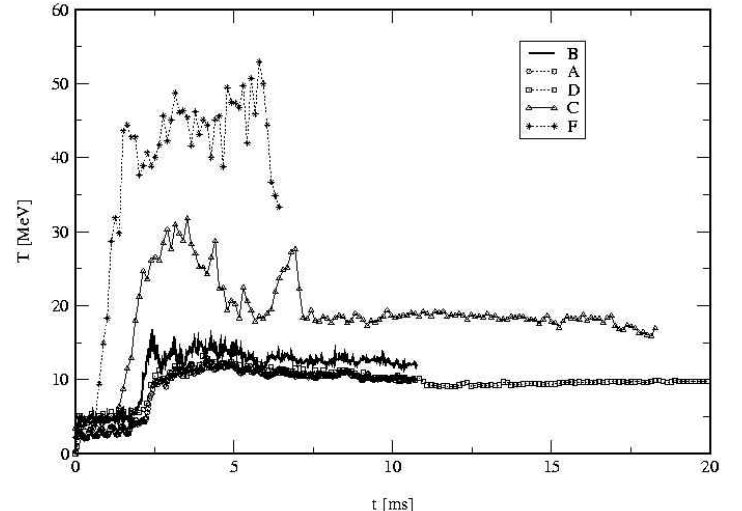


Figure 9. Maximum temperatures in the merged configurations.

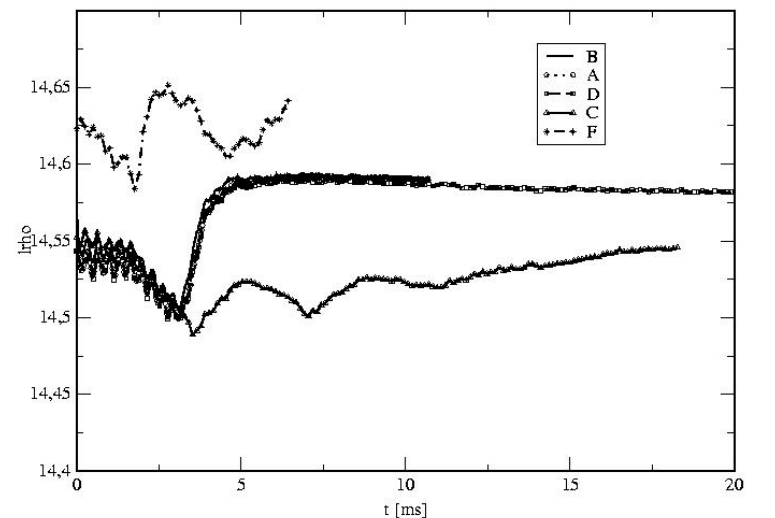


Figure 10. Maximum densities of the different runs. Shown is the $\log(\rho)$ with ρ in g cm^{-3} .

Figure 6. Left column: velocity field and density contours in the orbital plane in the corotating frame for an initially corotating configuration (> 1000000 particles). Shown is the central object only (down to $\log(\rho = 13.5, \rho \text{ in g cm}^{-3})$). Right column: corresponding temperatures.

Figure 7. Left column: velocity field and density contours in the orbital plane in the corotating frame for a system without spins (~ 400000 particles). Shown is the central object only (down to $\log(\rho = 13.5, \rho \text{ in g cm}^{-3})$). Right column: corresponding temperatures.

the merged configuration are found, see left columns Figs. 6 and 7. The hot spots reflect the dissipation inside the vortex structures. The maximum temperatures inside the central objects are shown in Fig. 9. In the case of corotation the temperature hardly rises above the level during inspiral, which is determined by a combination of imperfect initial conditions and numerical noise that translates into temperatures of a few MeV due to the degeneracy of the neutron star material. Due to the larger shear motion irrotational initial conditions yield substantially higher maximum temperatures: up to ~ 30 MeV in the case of $1.4 M_{\odot}$ and ~ 50 MeV for $2.0 M_{\odot}$ stars. These temperatures are lower than those reported by Ruffert et al. (1996). This is an effect of the different masses used in both investigations (1.4 versus $1.6 M_{\odot}$) and the different EOS (compare also Ruffert & Janka (2001), Fig. 15).

We find the masses of the central objects to be roughly $0.1 M_{\odot}$ lower, see Table 2, than those of previous calculations using the softer Lattimer-Swesty EOS (Rosswog et al., 1999).

Most state of the art nuclear equations of state can support cold, non-rotating neutron stars in beta-equilibrium of $\sim 2.2 M_{\odot}$ gravitational mass (Akmal et al., 1998). This corresponds approximately to the baryonic masses we find here for the central objects. Recent relativistic mean field equations of state are able to stabilize even heavier neutron stars (between 2.45 and $3.26 M_{\odot}$, (Chung et al., 2001)). Therefore even cold, non-rotating configurations of the masses found here may be supported by most EOSs. Stabilizing effects come from the finite, thermal contributions to the pressure. Additionally, the matter may contain non-leptonic negative charges such as Σ^- hyperons, d or s quarks, and under these conditions trapped neutrinos lead to an additional increase of the maximum mass (Prakash et al., 1995). The strong magnetic field of neutron stars may be substantially amplified by the differential rotation, see Fig 8, which, again, leads to a substantial increase of the maximum mass (Cardall et al., 2001). The possibly most important stabilizing effect, however, is the differential rotation of the remnant. The enormous increase in the maximum mass by differential rotation has been demonstrated for the case of white dwarfs by Ostriker & Bodenheimer (1968) who constructed configurations up to $4.1 M_{\odot}$. It may be somewhat bold to speculate from an essentially Newtonian calculation about the stability of the remnant, but from the above line of argumentation we are tempted to conclude that the *central object remains stable at least on the simulation time scale, ~ 20 ms*. This is further supported by the evolution of the maximum densities for the most probable, non-spinning case. Here the final densities are still below the density of a single neutron star.

Recent general relativistic treatments of differentially rotating neutron stars (Baumgarte et al., 2000) find that even

modest degrees of differential rotation allow for significantly higher maximum masses than non or uniformly rotating configurations.

3.4 Disk

A few milliseconds after contact a thick, hot torus has formed around the central object. It becomes shock heated during its formation process when the laterally expanding spiral arms hit supersonically. This heating mechanism is illustrated for a corotating system (run A) in Fig. 11.

Fig. 12 shows disk properties for the most realistic, non-spinning configuration. The shedded mass follows eccentric trajectories, resulting in a fast initial expansion and cooling phase during the outward motion (see panel one, column one in Fig. 12) and a subsequent compression when the motion is reversed and the inner parts start to fall back towards the central object (see panel one, column two in Fig. 12), against material that is still being shed and moving outwards. During this process the inner torus is heated via shocks and shear from the differential rotation to temperatures of 2-3 MeV (second panels column one and two of Fig. 12). This is substantially lower than the temperatures found by Ruffert & Janka (2001), who find maximum temperatures between 5 and 10 MeV. We suspect the stiffness of the Shen-EOS in the range between 10^{12} and $10^{14} \text{ g cm}^{-3}$, see Fig. 2, to be responsible for this fact.

Despite the high temperatures we still find a substantial mass fraction of heavy nuclei in the inner parts of the disk, which dominate the neutrino emission. We find roughly 10 % of the disk mass in the form of heavy nuclei (third panels in columns one and two of Fig. 12). The Shen-EOS yields in the inner torus regime an average nucleus with $A \sim 80$ and $Z \sim 0.3$. Using the neutrino cross sections from appendix A, we find for the ratio of the mean free path due to scattering off heavy nuclei, λ_A , and off free nucleons, λ_n , $\lambda_A/\lambda_n = n_n \sigma_n / (n_A \sigma_A) \approx 4(1 - X_h) / (X_h A) \approx 0.5$. Therefore *the scattering mean free path in these regions is dominated by heavy nuclei*. These have not been accounted for in previous investigations, which assumed the torus to be fully photodisintegrated (Ruffert et al., 1996), an assumption that may be justified for the higher temperatures encountered there.

4 SUMMARY AND DISCUSSION

We have performed high-resolution 3D calculations of the last moments of the inspiral and the final coalescence of a neutron star binary system. Our main motivation was to explore the impact of the, sometimes poorly known, micro-physics on the merger scenario.

The equations of hydrodynamics were solved using the

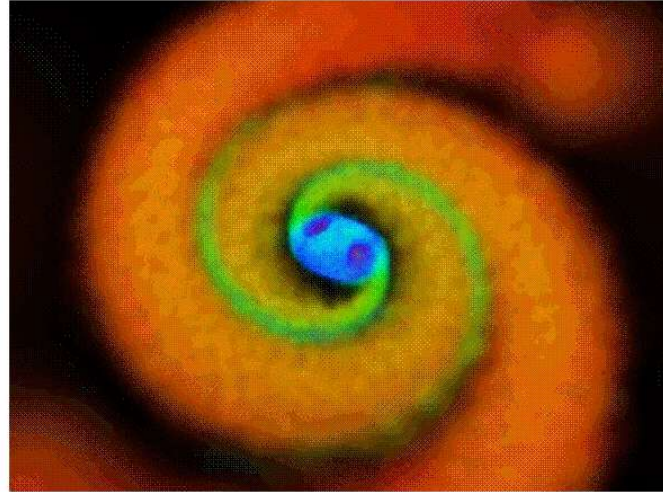


Figure 11. Disk heating mechanism: temperatures of the central region shortly after the merger (5.225 ms, corotation, ~ 200000 particles, run A). The disk is shock-heated when the spiral arms hit supersonically due to their lateral expansion. The two hot spots in the central object stem from the vortices which formed during the Kelvin-Helmholtz instability during the merger (see text).

Figure 12. Physical properties of the disk forming around the central object (no initial spins, run C).

smoothed particle hydrodynamics method with particle numbers of more than 10^6 to resolve the details of the thermodynamic and nuclear evolution. The initial neutron stars are resolved with smoothing lengths of ≈ 0.38 km. The self-gravity of the fluid was treated in a Newtonian fashion, but forces from the emission of gravitational waves were added. In these calculations the temperature-dependent, microscopic behaviour of the matter is modelled using a new nuclear equation of state whose baryonic part is described in the relativistic mean field approach (Shen et al., 1998a,b). We have added the contributions of electron-positron pairs (treated without any approximation) and photons to the baryonic component. In the low density regime the equation of state has been extended with a gas consisting of neutrons, alpha particles, electron-positron pairs and photons. This new EOS comprises the whole parameter space in density, temperature and electron fraction that is relevant to the neutron star merger scenario and therefore overcomes the restrictions inherent to previous calculations using a different equation of state (Ruffert et al., 1996; Rosswog et al., 1999).

We have also included the change in the electron fraction, Y_e , and internal energy due to the emission of neutrinos by means of a detailed neutrino leakage scheme that accounts carefully for the energy dependence of the neutrino reactions. In contrast to previous calculations scattering off heavy nuclei was included as a source of opacity.

The new equation of state is substantially stiffer than the previously used Lattimer-Swesty EOS, adiabatic exponents reaching values well above 3 within a $1.4 M_\odot$ star. This has several important implications. First, since the stars are less centrally condensed the binary system becomes dynamically unstable at a larger separation. Since the inspiral behaviour changes qualitatively at this point from a quasi-stationary, quasi-periodic motion to a dynamic “plunge” towards each

other the gravitational wave signal will change correspondingly at this point. For a corotating system of $1.4 M_\odot$ we find the instability to set in at a separation $a \approx 3.3 R_*$, corresponding to ~ 49 km and a frequency of ≈ 280 Hz, well within the range accessible to GEO600 and LIGO (Schutz & Ricci, 2001).

Once the neutron stars come into contact a Kelvin-Helmholtz unstable vortex sheet forms between both stars leading to the formation of vortex rolls. In the case of an initially corotating system two such vortices form which remain present and well-separated until the end of the calculation. In the more important irrotational case, several vortices form which merge within an orbital time scale leaving behind a differentially rotating central object. It is within these vortex roles that the highest temperatures of the merged configuration are found, reaching peak values of 30 MeV for the case of an irrotational system, while in the corotating case only a moderate temperature increase is observed. In a test calculation using two stars of $2.0 M_\odot$ temperatures of up to 50 MeV are reached. We find generally comparable but slightly lower temperatures than previous investigations that used the Lattimer-Swesty EOS. This is most pronounced in the dense inner torus around the central object where we find temperatures of 2-3 MeV as compared to 5-10 MeV in the Lattimer-Swesty case. Despite the high temperatures we find a substantial amount, a mass fraction of $\sim 10\%$, of heavy nuclei present even in the inner parts of the torus. This is enough to dominate the neutrino scattering opacities which therefore play a crucial role for the neutrino transport. This has important consequences for the enormously temperature sensitive neutrino reactions and will be discussed in a future paper.

The masses of the central objects are roughly $0.1 M_\odot$ lower than in previous calculations where we used the Lattimer-Swesty-EOS, leading to masses of the central object that

are comparable to the maximum masses that most recent nuclear equations of state can support for cold, non-rotating configurations. Since several stabilizing effects like thermal pressure contributions, rotation and, most likely, magnetic fields are active during the coalescence, we suspect the central object will remain stable on at least the simulation time scale of 20 ms. Probably the most important stabilisation comes from differential rotation. For the most probable case, where the neutron star spins are negligible with respect to the orbital motion, the maximum density of the central object barely reaches the initial central density of a single neutron star although its mass is roughly one solar mass higher. It has to be stressed, however, that none of the above quoted equations of state contains particles more exotic than nucleons. The appearance of more exotic matter in the deep cores of neutron stars is still subject to large uncertainties due to poorly constrained many-body interactions at highest densities. Therefore final conclusions on this point cannot be drawn.

If the central object indeed remains stable for several 10 ms the initial magnetic fields may wind up to reach $\sim 10^{17}$ G for a typical rotation period of 2 ms (Duncan & Thompson, 1992) and may therefore provide the conditions for magnetically-powered gamma ray bursts.

Acknowledgements

It is a pleasure to thank the Leicester supercomputer team Stuart Poulton, Chris Rudge and Richard West for their excellent support.

Most of the computations reported here were performed using the UK Astrophysical Fluids Facility (UKAFF). Part of this work has been performed using the University of Leicester Mathematical Modelling Centre's supercomputer which was purchased through the EPSRC strategic equipment initiative.

This work was supported by a PPARC Rolling Grant for Theoretical Astrophysics. MBD gratefully acknowledges the support of the Royal Society by a URF.

References

Abramovici A., Althouse W. E., Drever R. W. P., Gursel Y., Kawamura S., Raab F. J., Shoemaker D., Sievers L., Spero R. E., Thorne K. S., 1992, *Science*, 256, 325

Akmal A., Pandharipande V., Ravenhall D., 1998, *nucl-th/9804027*

Ayal S., Piran T., Oechslin R., Davies M. B., Rosswog S., 2001, *ApJ*, 550, 846

Balsara D., 1995, *J. Comput. Phys.*, 121, 357

Baumgarte T., Cook G., Scheel M., Shapiro S., Teukolsky S., 1997, *Phys. Rev. Lett.*, 79, 1182

Baumgarte T., Cook G., Scheel M., Shapiro S., Teukolsky S., 1998a, *Phys. Rev. D*, 57, 6181

Baumgarte T., Cook G., Scheel M., Shapiro S., Teukolsky S., 1998b, *Phys. Rev. D*, 57, 7299

Baumgarte T., Shapiro S., Shibata M., 2000, *ApJ*, 528, L29

Benz W., 1990, in Buchler J., ed., *Numerical Modeling of Stellar Pulsations*. Kluwer Academic Publishers, Dordrecht, p. 269

Benz W., Bowers R., Cameron A., Press W., 1990, *ApJ*, 348, 647

Bildsten L., Cutler C., 1992, *ApJ*, 400, 175

Bradacchia C. et al., 1990, *Nucl.Instrum. Methods Phys. Res. A*, 289, 518

Cardall C., Prakash M., Lattimer J., 2001, *ApJ*, 554, 332

Chandrasekhar S., 1975, *ApJ*, 202, 809

Chung K., Wang C., Satiago A., Zhang J., 2001, *astro-ph/0102993*, 0, 0

Danzmann K., 1997, in of Sciences T. N. Y. A., ed., *Proceedings of the 17th Texas Symposium on relativistic astrophysics and cosmology* New York

Davies M. B., Benz W., Piran T., Thielemann F.-K., 1994, *ApJ*, 431, 742

Duncan R., Thompson C., 1992, *ApJ*, 392, L9

Eichler D., Livio M., Piran T., Schramm D. N., 1989, *Nature*, 340, 126

Faber J., Rasio F., 2000, *Phys.Rev. D*62, p. 064012

Faber J., Rasio F., Manor J., 2001, *Phys.Rev. D*63, p. 044012

Font J., Dimmelmeier H., Gupta A., Stergioulas N., 2000, *astro-ph/0012477*

Freiburghaus C., Rosswog S., Thielemann F.-K., 1999, *ApJ*, 525, L121

Heap S., Corcoran M., 1992, *ApJ*, 387, 340

J.H. van Kerkwijk J. v. P., Zuiderwijk E., 1995, *A&A*, 303, 497

Kochanek C., 1992, *ApJ*, 398, 234

Kuroda K. et al., 1997, in *Gravitational Wave Detection, Proceedings of the TAMA International Workshop on Gravitational Wave Detection* held at National Women's Education Centre, Saitama, Japan, on 12-14 November, 1996. Edited by K. Tsubono, M.-K. Fujimoto, and K. Kuroda. Frontiers Science Series No. 20. Universal Academy Press, Inc., 1997., p.309 Japanese gravitational wave observatory (jgwo). pp 309+

Lai D., 1994, *MNRAS*, 270, 611

Lai D., Rasio F., Shapiro S., 1994a, *ApJ*, 420, 811

Lai D., Rasio F., Shapiro S., 1994b, *ApJ*, 423, 344

Lattimer J. M., Schramm D. N., 1974, *ApJ*, (Letters), 192, L145

Lattimer J. M., Schramm D. N., 1976, *ApJ*, 210, 549

Lattimer J. M., Swesty F. D., 1991, *Nucl. Phys.*, A535, 331

Monaghan J., 1992, *Ann. Rev. Astron. Astrophys.*, 30, 543

Monaghan J., Gingold R., 1983, *J. Comp. Phys.*, 52, 374

Morris J., Monaghan J., 1997, *J. Comp. Phys.*, 136, 41

Oechslin R., Rosswog S., Thielemann F.-K., 2001, in preparation

Oohara K., Nakamura T., 1997, in *Relativistic Gravitation and Gravitational Radiation*. Cambridge University Press, Cambridge

Orosz J., Kuulkers E., 1999, *MNRAS*, 305, 132

Ostriker J., Bodenheimer P., 1968, *ApJ*, 151, 1089

Paczynski B., 1986, *ApJ*, 308, L43

Prakash M., Cooke J., Lattimer J., 1995, *Phys. Rev.*, D52, 661

Rasio F., Shapiro S., 1992, *ApJ*, 401, 226

Rasio F., Shapiro S., 1994, *ApJ*, 432, 242

Rasio F., Shapiro S., 1995, *ApJ*, 438, 887

Rasio F., Shapiro S., 1999, *Class. Quant. Grav.*, 16, R1

Rosswog S., Davies M. B., Thielemann F.-K., Piran T., 2000, *A & A*, 360, 171

Rosswog S., Liebendörfer M., Ramirez-Ruiz E., Davies M. B., 2001, in preparation

Rosswog S., Liebendörfer M., Thielemann F.-K., Davies M. B., Benz W., Piran T., 1999, *A & A*, 341, 499

Ruffert M., Janka H., 2001, *astro-ph/0106229*

Ruffert M., Janka H., Schäfer G., 1996, *A & A*, 311, 532

Ruffert M., Janka H., Takahashi K., Schäfer G., 1997, *A & A*, 319, 122

Schutz B., Ricci F., 2001, Gravitational Waves, 1. edn. IoP, London

Shapiro S., Teukolsky S. A., 1983, Black Holes, White Dwarfs and Neutron Stars. Wiley & Sons, New York

Shen H., Toki H., Oyamatsu K., Sumiyoshi K., 1998a, *Nuclear Physics A* 637, 435

Shen H., Toki H., Oyamatsu K., Sumiyoshi K., 1998b, *nuclear Physics A* 637, 435

Shibata M., 1999, *Phys. Rev. D*, 60, 104052

Shibata M., Uryu K., 2000, *Phys. Rev. D*, 61, 064001

Shibata M., Uryu K., 2001, *astro-ph/0104409*

Sugahara Y., Toki H., 1994, *Nucl. Phys.* A579, 557

Symbalisty E. M. D., Schramm D. N., 1982, *Astrophys. Lett.*, 22, 143

Tassoul M., 1975, *ApJ*, 202, 803

Tassoul M., 2001, Stellar Rotation. Cambridge University Press, Cambridge

Taylor J., 1994, *Rev. Mod. Phys.*, 66, 711

Thorsett S., Chakrabarti D., 1999, *ApJ*, 512, 288

Timmes F., Arnett D., 1999, *ApJS*, 125, 277

Wilson J. R., Mathews G., 1995, *Phys. Rev. Lett.*, 75, 4161

Zhuge X., Centrella J., McMillan S., 1994, *Phys. Rev. D* 50, 6247

Zhuge X., Centrella J., McMillan S., 1996, *Phys. Rev. D* 54, 7261

This figure "NSMI_fig5.gif" is available in "gif" format from:

<http://arxiv.org/ps/astro-ph/0110180v1>

This figure "NSMI_fig6.gif" is available in "gif" format from:

<http://arxiv.org/ps/astro-ph/0110180v1>

This figure "NSMI_fig7.gif" is available in "gif" format from:

<http://arxiv.org/ps/astro-ph/0110180v1>

This figure "NSMI_fig12.gif" is available in "gif" format from:

<http://arxiv.org/ps/astro-ph/0110180v1>